energies

MDPI

Article

Measurement of a Three-Dimensional Rotating Flow Field and Analysis of the Internal Oil Droplet Migration

Lei Xing [1,3,4], Shuai Guan [1,3], Yang Gao [2,*] and Minghu Jiang [1,3]

1 School of Mechanical Science and Engineering, Northeast Petroleum University, Daqing 163318, China; nepuxinglei@163.com (L.X.)
2 China Research Institute of Petroleum Exploration and Development, CNPC, Beijing 100000, China
3 Heilongjiang Key Laboratory of Petroleum and Petrochemical Multiphase Treatment and Pollution Prevention, Northeast Petroleum University, Daqing 163318, China
4 Postdoctoral Research Workstation in Daqing Oilfield, Daqing 163318, China
* Correspondence: gaoyang573@163.com; Tel.: +86-459-6504050

Abstract: Investigating the motion of discrete oil droplets in a rotating flow field can provide a theoretical basis for optimizing the flow field and structural parameters of hydrocyclones and centrifugal separation equipment. In the present work, the particle image velocimetry (PIV) method was applied to study the velocity distribution of a three-dimensional axial-rotor-driven rotating flow field and the influence of the velocity distribution of different rotor speeds on the flow field. The radial migration of oil droplets with different particle sizes in the rotating flow field was visually analyzed using high-speed video (HSV). The results showed that the oil droplets with the same radial position had diameters of 2.677 and 4.391 mm, whereas the movement times to the axis were 0.902 and 0.752 s. The larger the oil droplet size, the shorter the time to move to the axial center of the rotating flow field. The radial velocities of oil droplets with diameters of 2.677 and 2.714 mm were 0.0221 and 0.02 $m \cdot s^{-1}$, respectively. In addition, a mathematical expression was established between the radial migration time and the oil droplet size in the rotating flow field. The accuracy of the proposed expression was verified using experiments.

Keywords: rotating flow field; oil droplet; PIV; velocity; diameter

check for updates

Citation: Xing, L.; Guan, S.; Gao, Y.; Jiang, M. Measurement of a Three-Dimensional Rotating Flow Field and Analysis of the Internal Oil Droplet Migration. *Energies* **2023**, *16*, 5094. https://doi.org/10.3390/en16135094

Academic Editor: Albert Ratner

Received: 25 May 2023
Revised: 15 June 2023
Accepted: 18 June 2023
Published: 1 July 2023

1. Introduction

Multiphase flows are one of the common flows that are abundant in nature and industrial processes such as transportation of energy carriers, chemical reactions, and designing aviation parts. The dynamic and kinematic characteristics of the discrete phase may significantly affect the performance of industrial equipment such as cyclone separators [1], fluidized beds [2], and jet reactors [3]. Therefore, the motion behavior of the discrete phase should be taken into account in the calculation. The discrete phase has a series of dynamic behaviors in the flow field, including coalescence settlement [4], deformation [5], and crushing [6]. Recently, investigation of the motion characteristics of the discrete phase has attracted the attention of many scholars and become a research hotspot [7–9].

Dalgamoni et al. [10] combined the axisymmetric lattice Boltzmann method with theoretical analysis to study the motion behavior of the discrete phase in a two-dimensional flow field. Moreover, the collisions of droplets with different Weber numbers, radii, and surface wettability were also studied. It was found that the motion of particles can be classified into five categories: deposition, partial bounce, partial bounce and satellite droplets, total bounce, and total bounce and satellite droplets. Yuan et al. [11] numerically simulated the binary nonconcentric collision of equal-diameter water droplets in the oil phase, analyzed the formation mechanism, and proposed a theory for the collisions of droplets under different parameters. To study the motion of the discrete phase in a three-dimensional flow field, Wu et al. [12] used the visualization experimental method to compare and analyze the motion characteristics of bubbles in the rising process and analyzed the rising and evolution of bubbles under different nozzle immersions. Moreover, the variation of shape and equivalent diameter of bubbles was analyzed. Zhang et al. [13] adopted a numerical method to simulate a standard cyclone separator, tracked the trajectory of particles, and simulated the trajectory of solid particles with a certain diameter in a cyclone separator under different inlet velocities and angles. Furthermore, Solsvik [14] used high-speed video imaging technology and studied the dynamic transport of toluene, n-dodecane, and octanol in turbulent distilled water in a stirred tank. Liu et al. [15] applied the three-phase lattice Boltzmann model to study the dynamic transport behavior of composite droplets under the action of three-dimensional oscillatory shear flow. In this regard, the effects of the oscillation period, internal and external fluid viscosity, wall constraint, and the number of capillaries (Ca) on the behavior of composite droplets were studied. Ling et al. [16] performed numerical simulations and studied the effects of a pulsating airflow on the droplet-breaking process and established a three-dimensional model to simulate the transverse airflow. Then, the deformation rate of the droplets was analyzed under different amplitudes and frequencies. Sun et al. [17] studied the shear-driven deformation and creeping of silicone oil droplets under different viscosities from the point of view of mechanics. Based on the two-phase lattice Boltzmann model, Bhardwaj [18] studied the deformation and fracture dynamics of liquid droplets passing through an obstacle. It is worth noticing that the reviewed studies were based on dynamic changes of the discrete phase in the flow field and laid a theoretical foundation for subsequent studies on the motion behavior of the discrete phase in the flow field. The dynamic discrete phase in a three-dimensional rotating flow field has been mostly studied in hydrocyclones [19]. Yuan et al. [20] analyzed the force, coalescence mechanism, and process of the dispersed phase droplets in hydrocyclones through experiments and theoretical analyses. Chen et al. [21] established the numerical model of a fluid in hydrocyclones using computational fluid dynamics (CFD) and porous media model and numerically simulated and analyzed the distributions of the velocity and pressure fields in a large cone gas injection cyclone. Wang et al. [22] used the discrete phase model to simulate the motion of oil droplets in a hydrocyclone and analyzed the movement trajectory of oil droplets. Xu et al. [23] used large eddy simulation (LES) and the Reynolds stress model (RSM) to simulate the flow field in a cyclone separator and obtained the distribution of velocity, turbulence intensity, and vorticity on different sections. Xie et al. [24] conducted experiments and investigated the flow of conventional-scale bubbles with low gas content gas–liquid in the cyclone separation process and analyzed the effects of inlet flow rate on the separation performance and bubble motion.

The migration dynamics of droplets in the rotating flow field has been investigated by the numerical simulation method. However, there are few reports on the systematic analysis of the dynamic behavior of discrete droplets in a three-dimensional rotating flow field by experimental methods. The mechanical behavior mechanism of discrete oil droplet migration in the rotating flow field has not yet been clearly revealed. The literature survey that was performed indicates that numerous analyses have been conducted to investigate the motion of discrete phase in a three-dimensional rotating flow field. In this paper, the velocity field of the rotating flow field produced by a magnetic agitator was measured using particle imaging velocimetry (PIV), and distributions of radial, axial, and tangential velocities were obtained. A high-speed video (HSV) was used to construct a visual experimental system and study the motion of discrete oil droplets in the rotating flow field. The main objective of the present study was to analyze the settling process and the influencing factors on oil droplets in the swirling field. The results of this article can provide a theoretical reference for designing efficient cyclone separation equipment and obtaining optimal parameters for their design. The results of this manuscript have academic reference value in revealing the transport mechanism of discrete phase oil droplets in rotating flow fields. In addition, the research results provide a theoretical basis for guiding the design of high-efficiency oil–water separation equipment.

2. Experimental

2.1. PIV Experiments

Particle image velocimetry (PIV) is a method that is widely used to measure transient noncontact parameters in multiple points and obtain the spatial characteristics of the flow field in real time [25,26]. Accordingly, this method was applied to study the velocity field of a three-dimensional rotating flow field. The PIV experimental system is shown in Figure 1a. The positional arrangement of the camera and light source is shown in Figure 1b. The parameters of the rotating flow field is shown in Figure 1c. The experimental system mainly consisted of a laser pulser (Dual Power 20015, Shanghai, China), a charge-coupled device (CCD) camera (Flow Sense EO 4M, Shanghai, China) with a resolution of 2048 × 2048 pixels and a maximum frequency of 20 Hz, a sheet lens group, a synchronizer, a visualization software (i-SPEED Control Software Suite 2.0), an image data processing system, and a magnetic agitator. A 1000 mL beaker was used in the swirling field. The radius and height of the fluid domain were 53 and 100 mm, respectively, and the rotational diameter of the rotor was 25 mm. When measuring the velocity of the flow field, the laser was generated by a double-pulse laser generator. After passing through the controller, the light guide arm, and the lens of the light source, the laser beam irradiated the area to be tested in the form of a sheet light. According to the experimental conditions, the thickness and intensity of the laser were adjusted by adjusting the controller. Laser scattering occurred on the tracer particles, which were uniformly distributed in the flow field. Meanwhile, the motion image of the tracer particles was obtained using the charge-coupled camera (CCD), which was installed perpendicular to the cross section of the flow field. The relationship between the particle displacement and time was determined using the cross-correlation algorithm. The image data were expressed as two-dimensional discrete signals x[m,n] and y[m,n], and the cross-correlation function was defined by Equation (1) [27]:

$$R_{xy}[j,k] = \sum_{m=0}^{M-1} \sum_{n=0}^{N-1} x[m,n]y[m+j,n+k] \tag{1}$$

where $j = 1, 2, 3, \ldots, M-1$, and $k = 1, 2, 3, \ldots, N-1$. The image size was $M \times N$, where $x[m, n]$ and $y[m, n]$ denote the function of the image in t_1 and $t_1 + \Delta t$ time interpretation areas, respectively. Moreover, $y[m, n]$ is the shape of $x[m, n]$ after time Δt. It is worth noticing that the larger the degree of similarity of the image window corresponding to $x[m, n]$ and $y[m, n]$, the larger the corresponding value of $R_{xy}[j, k]$. When the value of $R_{xy}[j, k]$ reached the maximum, the relative displacement of the interpretation area $x[m, n]$ after time Δt was obtained and the particle microcluster velocity at a specific time was calculated.

(**a**)

Figure 1. *Cont.*

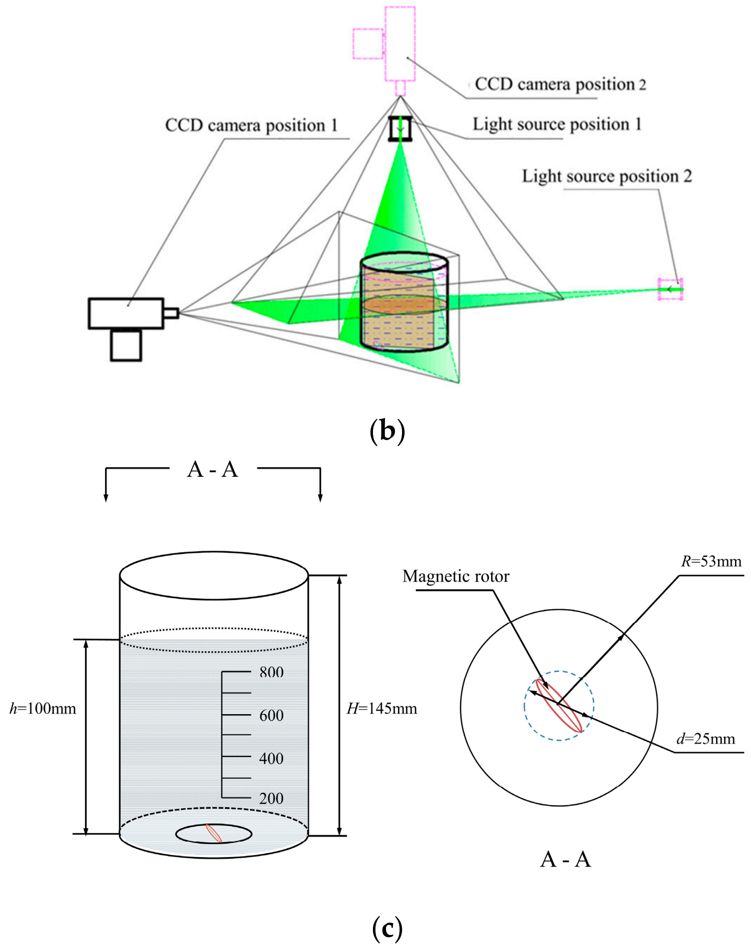

Figure 1. Configuration of the PIV experimental setup and process arrangements under different working conditions. (**a**) Position arrangement of experimental equipment. (**b**) Position arrangement of experimental equipment. (**c**) Parameters of the rotating flow field.

2.2. HSV Experiments

In order to analyze the radial settling velocity and obtain the settling distance and time of oil droplets with different particle sizes at different positions, the motion of the oil droplets was captured in the swirling field. Figure 2 shows that the high-speed video analysis system was mainly composed of a high-speed video (Olympus's I-speed-3-T2 series, Tokyo, Japan) with a frame rate of 150,000 frames per second, a magnetic agitator, a shading plate, and a light source. The video image was observed and analyzed by i-SPEED suite software. The magnetic agitator could induce stirring at the rate of 0–2040 r/min, whereas the temperature range of the flow field was 0–100 °C. Moreover, the shaft length of the magnetic rotor was 25 mm. Due to the high speed of particles in the flow field, the light was strengthened at various frame rates. The power provided to the light was 1000 W, and the light intensity was adjustable. The shading board was a high-transmission whiteboard, which was used to weaken the light intensity and make the light illumination uniform within the swirling field to improve the clarity of the picture captured in the high-speed video. Distilled water was utilized to form the rotating flow field, and the density and viscosity of the distilled water was 998 kg/m^3 and 1.003×10^{-3} Pa·s, respectively. The oil droplets were prepared with heavy-duty gear oil (GL-585W-90, Great Wall, Shanghai, China) with viscosity of 1.03 Pa·s at 25 °C and density of 850 kg/m^3, which is similar to crude oil.

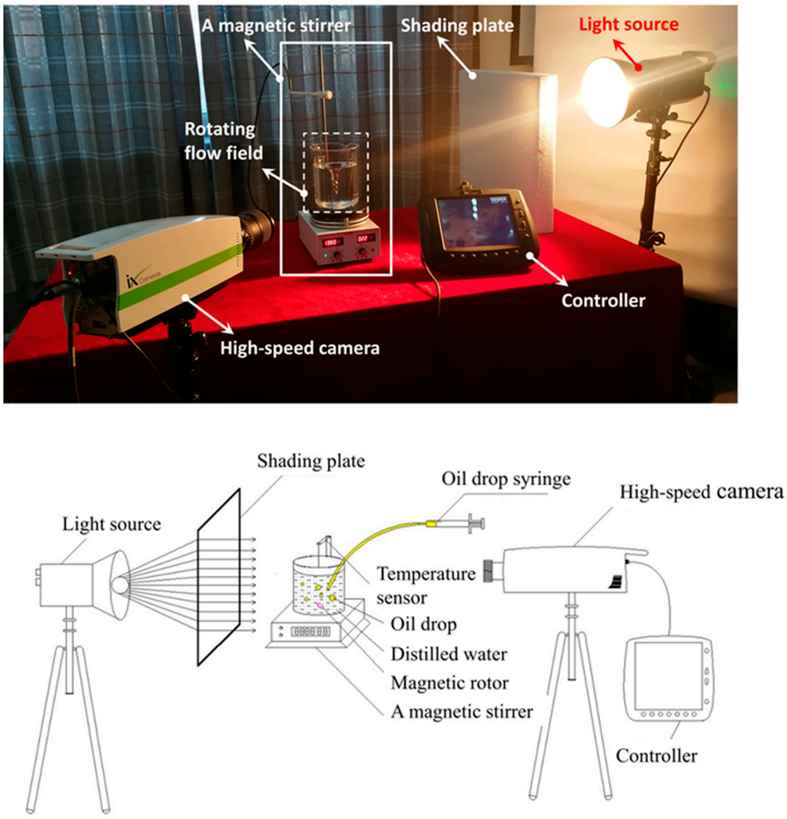

Figure 2. HSV experimental equipment and process layout.

Oil droplets were injected into the rotating flow field using a syringe. In this regard, different syringes with different capacities were selected to control the size of the oil droplets.

3. Results and Discussion

3.1. Analysis of the Velocity of the Rotating Flow Field Based on PIV

3.1.1. Characteristics of Axial and Radial Velocity Distributions

In this section, the experimental results of the axial area of the swirling field at 1040 r/min are presented. Figure 3a shows the captured axial cross section of the flow field and the position and morphology of the gas core. When analyzing the measurement results, the analysis area was selected as shown by the area in red in Figure 3a. To obtain the velocity data at different positions on the axial section, the axial and radial velocities were extracted according to the position shown by sections I–VI. Figure 3b shows the velocity vectors superimposed on the velocity contour. It was observed that the radial velocity of the flow field near the edge of the gas core gradually increased on the axial analysis section of the rotating flow field, and the maximum value was 0.2 m/s. In the region near the gas core, the flow field moved upwards both axially and radially. However, there was no clear pattern in the distribution of axial and radial velocities in other regions. As shown in Figure 3b, there was an obviously derived eddy current in the axial cross section. Moreover, there were more eddy currents in the area far from the center of the flow field, and the derived eddy current in the region near the axial gas core obviously decreased.

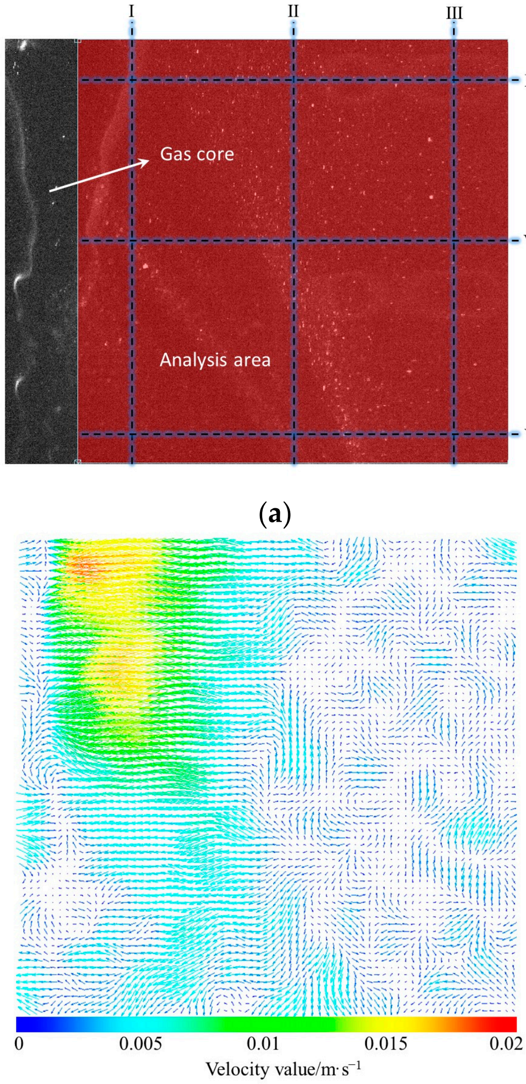

(**a**)

(**b**)

Figure 3. Selection of analysis area and velocity vectors of the axial analysis section. (**a**) Selection of the analysis area. (**b**) Velocity vectors of the axial analysis section.

In order to accurately measure and analyze the velocity distribution of the flow field, the radial velocity distribution data of the truncated positions I–III were obtained, and the results are shown in Figure 4a. It was found that the radial velocity of the truncated line I near the gas core decreased gradually from top to bottom, while there was no set variation pattern in truncated lines II and III. Meanwhile, the radial velocity fluctuated within the range of less than 0.005 $m \cdot s^{-1}$. The axial velocity distributions at positions IV, V, and VI are shown in Figure 4b. It was observed that there was no obvious variation pattern in the axial velocity distribution at the analysis position. Moreover, there was no obvious variation pattern in the radial and axial velocity distributions on the axial section of the flow field. This was because the density of tracer particles in the PIV experiment was the same as that of water, and the tangential rotational motion in the swirling field was the dominant motion of the medium. Furthermore, the centrifugal force, radial resistance, and random force of the tracer particles in the flow field were the same as those of the fluid medium. Consequently, the radial and axial velocity distributions were quite random. However, due to the random characteristics of the flow field, there was a derived eddy current along the axial direction.

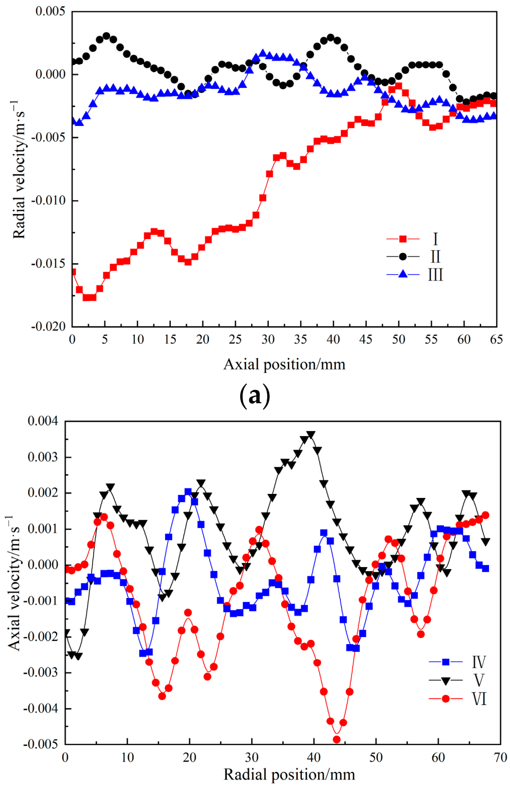

Figure 4. Radial and axial velocity distributions in the flow field. (**a**) Radial velocity. (**b**) Axial velocity.

3.1.2. Characteristics of Axial and Radial Velocity Distributions

In order to obtain the tangential velocity data of the target flow field, the tangential velocity distribution of the flow field was measured and analyzed such that the CCD camera was located in position 2. During the measurement, the rotor speed was varied with values of 850, 1040, 1260, 1490, 1860, and 2050 r/min, and the influence of different rotor speeds on the tangential velocity distribution of the flow field was obtained. The cross-sectional image obtained by CCD during the measurement was used for tangential analysis. In order to facilitate the analysis, the analysis cross section was divided into two zones: the gas core disturbance zone and the stable zone. The dotted line in the diagram represents the analysis cross section, while the velocity data on the cross section was extracted for further analysis. The position of the gas core can be clearly seen in Figure 5. It was found that the larger the tangential velocity distribution of the flow field around the gas core, the larger the velocity gradients and the more stable the tangential velocity far from the gas core. The direction of the flow field also showed obvious rotational motion around the center of the gas core. In order to quantitatively analyze the velocity value on the tangential section, the velocity projection was calculated on the section that radially passed through the stable zone and the center of the gas core. The distributions of tangential, radial, and resultant velocities are shown in Figure 6. It was observed that in the gas nucleus disturbance zone, the farther from the center of the gas core, the greater the tangential velocity. However, in the stable zone, the greater the distance from the axis, the smaller the tangential velocity. It should be noted that during the measurement, the tracer particles could not be photographed continuously and clearly in the gas core region. Due to this reason, it was challenging to ensure the accuracy of measurements in this area. Therefore, the measurement results of the stable region were taken as the analysis object. As shown in Figure 6, the radial velocity did not change in the stable area, and the tangential and closing velocities decreased gradually along the axis. This was because the tangential rotation of the flow field mainly originated from the high-speed magnetic rotor, and therefore, the closer to the rotor, the higher the tangential velocity of the fluid.

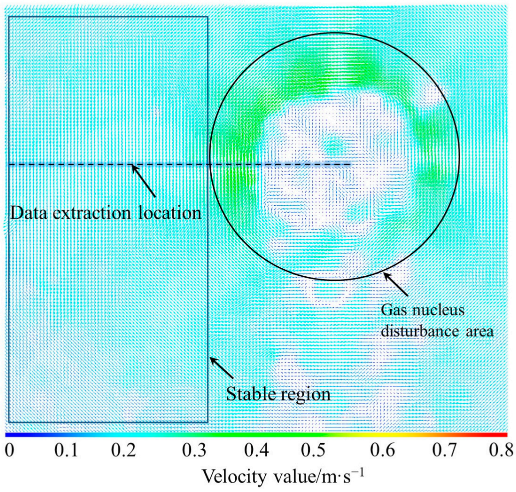

Figure 5. Cross-sectional velocity vectors at a rotating speed of 1020 r/min.

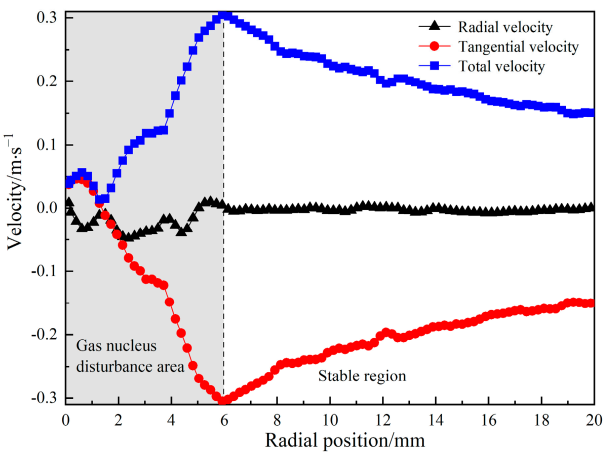

Figure 6. Velocity distribution at the cut-off position.

In order to compare the influence of different rotor speeds on the velocity field, different rotational speeds, namely, 850, 1040, 1260, 1490, 1860, and 2050 r/min, were considered in the experiments. The fluid trace of the tangential section of the flow field at different speeds was compared, and the corresponding results are shown in Figure 7. Based on the analysis of the trace diagram, the size and the position of the gas core were calculated. The analyses indicated that as the rotor speed increased, the gas core gradually increased. Meanwhile, the fluid trace in the gas core disturbance area became more chaotic, and the stable area in the analysis range gradually shrank. Moreover, the velocity contour indicated that as the rotor speed increased, the velocity of the gas core in the disturbance stable zones increased. The position of the cut-off line was analyzed using the data shown in Figure 5, and the angular velocity on the analysis section at different rotational speeds was analyzed. The obtained angular velocity contrast curve shown in Figure 8 demonstrated that when the rotational speed was 850 r/min, the disturbance radius of the gas core disturbance zone was about 6 mm and it increased with the increase in rotational speed. When the rotational speed was 2050 r/min, the disturbance radius of the gas core was 15 mm. Moreover, it was observed that in the stable region of the flow field, the angular velocity of the flow field gradually increased with the increase in rotational speed, while it decreased slowly along the radial direction.

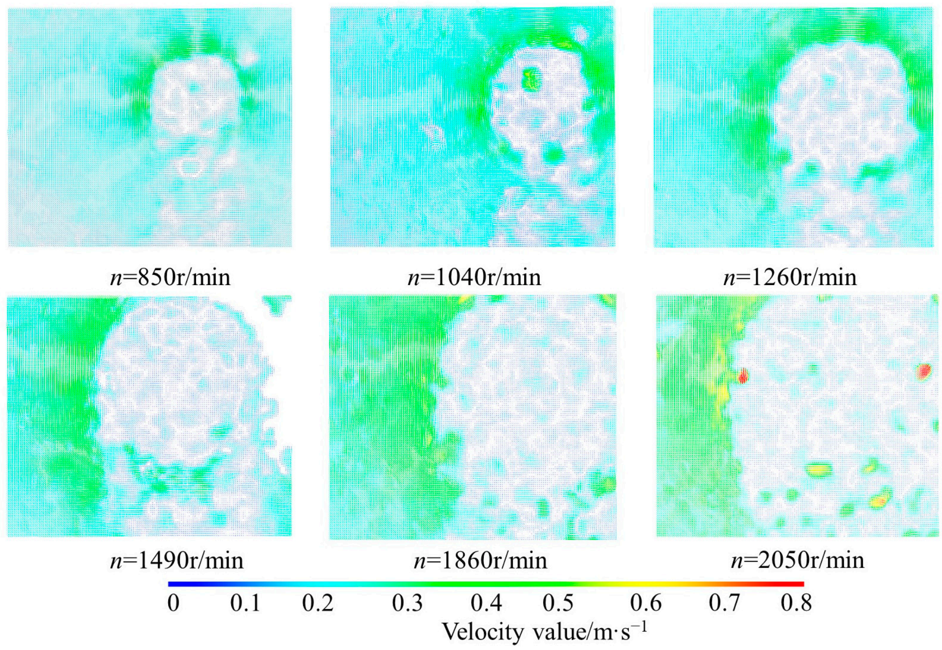

Figure 7. Comparison of tangential velocities at different rotational speeds.

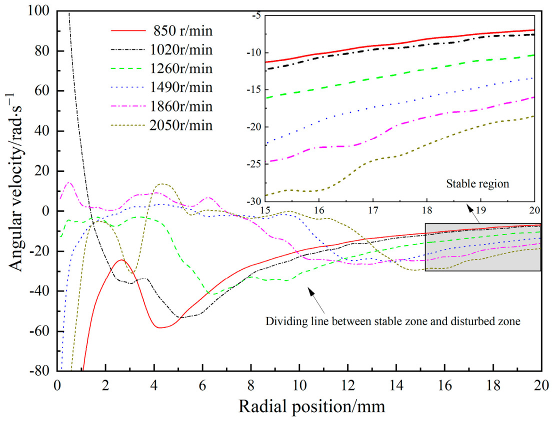

Figure 8. Angular velocities on the cut-off line at different rotational speeds.

The velocity data of the stable region of the flow field at different rotational speeds were selected for comparative analysis, and the tangential velocities of the flow field in the stable region at different rotational speeds are presented in Figure 9. It was observed that the tangential velocity in the stable region decreased gradually along the radial position. When the rotational speed was 850 r/min, the tangential velocity decreased from 0.275 to 0.15 m·s^{-1} along the radial direction. When the rotational speed increased to 2050 r/min, the tangential velocity varied within the range of 0.425–0.375 m·s^{-1}. It was found that as the rotational speed increased, the tangential velocity increased remarkably in the stable region. In order to accurately describe the variation of tangential velocity with radial distance in the stable zone, the exponential form of the tangential velocity as a function of radial distance was obtained by fitting the measured tangential velocity at different rotational speeds. The fitted curves and the corresponding equations are shown in Figure 9. In each fitting function, the independent variable x denotes the radial position, whereas the dependent variable y is the tangential velocity value. The analysis results and the coefficient of determination (R^2) showed that there was a high correlation between the fitting equation and the experimental data at different rotational speeds, demonstrating that the fitting function corresponding to different rotational speeds could be used to characterize the tangential velocity distribution of the flow field in the stable region.

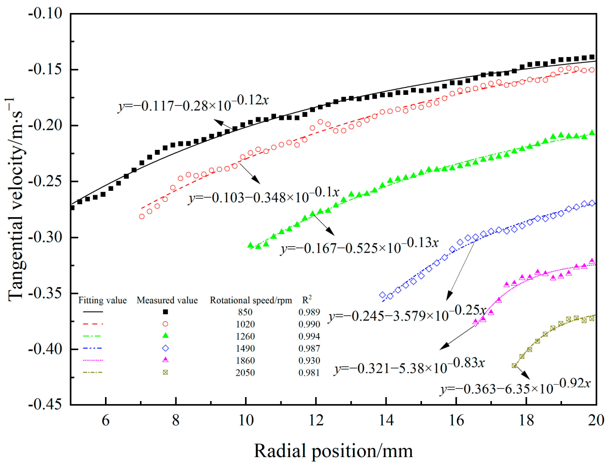

Figure 9. Tangential velocity fitting results in stable regions at different speeds.

3.2. Radial Migration of Oil Droplets in the Rotating Flow Field

The results showed that the flow field had a free vortex distribution, and the oil droplets in the discrete phase rotated around the axis in three dimensions. During the rotational motion, under the action of radial force, the rotation radius of the oil droplets gradually decreased [28]. Finally, the radial motion stopped at the axial position. Because the magnetic stirring flow field was complex, it was a three-dimensional strong shear turbulent motion. The analysis of the experimental data revealed that there were a large number of secondary-derived eddies in the axial direction. When a droplet encounters the derived vortex, the trajectory may deflect and stay stationary or rotate in the derived vortex [29–31]. Consequently, the stability of the flow field greatly affects the motion of the dispersed phase oil droplets. It was assumed that there was no derived eddy current in the flow field, and the radial motion of oil droplets was not affected by the random characteristics of the flow field. In this case, the resultant force of the oil droplet along the radial motion is expressed using Equation (2) [20]:

$$\sum F = F_\text{p} + F_\text{M} - F_\text{a} - F_\text{s} \tag{2}$$

where F_a is the centrifugal force pointing to the side wall of the flow field and hindering the movement of oil droplets to the axis, and F_p is the radial force originating from pressure. Under the action of the axial magnetic rotor, the rotating flow field amplified the rotational speed of the fluid in the axial region, thereby decreasing the pressure from the side wall to the axial flow field. The pressure difference along the radial direction pushed the oil droplet along the axial direction. When the oil droplet has a relative radial motion to the continuous phase medium, the viscosity of the continuous phase medium will hinder the movement of the oil droplet. Under this circumstance, the oil droplet was subjected to the viscous force away from the axis. This force is called the Stokes force and represented by F_s [32]. Analysis of the radial motion of the oil droplets showed that the droplets rotated in the rotating flow field. Moreover, the fluid above the oil droplet rotated in the same direction as the droplet, while the fluid below the oil droplet rotated in the opposite direction. Subsequently, the fluid velocity above the oil droplet increased, while the fluid velocity below it slowed down. Due to the pressure difference between the oil droplets, the droplets were subjected to a bottom-up force, which is called the Magnus force and represented by F_M [33].

The differential equation of the radial motion of oil droplets is given by Equation (3) [20]:

$$m_\text{o} \frac{dv_\text{r}}{dt} = F_\text{p} - F_\text{a} + F_\text{M} - F_\text{s} \tag{3}$$

where m_o is the oil droplet quality (kg), and v_r is the relative velocity of oil droplet and continuous phase (m/s). Equation (3) is written as Equation (4):

$$\frac{dv_r}{dt} = \frac{v_t^2}{r}\frac{\rho_w - \rho_o}{\rho_o} + \frac{6k\rho_w\omega \cdot v_r}{\pi\rho_o} - \frac{18v_r\mu_w}{x_o^2\rho_o} \quad (4)$$

where ρ_w is the density of water (kg/m^3), ρ_o is the density of oil (kg/m^3), μ_w is the viscosity of water (Pa·s), k is a constant, ω is the angular velocity of rotation of the oil droplets (m/s), v_t is the tangential velocity of the flow field, r is the radial distance between the position of the oil drop and the axis (m), and x_o is the oil droplet size (m).

When the force on the oil droplet was balanced, the following conditions were satisfied: $\sum F = 0$ and $\frac{dv_r}{dt} = 0$. In this case, the radial velocity of an oil droplet is calculated by Equation (5):

$$v_r = \frac{v_t^2}{r}\frac{(\rho_w - \rho_o)\pi x_o^2}{18\mu\pi - 6k\rho_w\omega \cdot x_o^2} \quad (5)$$

where $\Delta\rho = \rho_w - \rho_o$. The radial velocity of the oil drop is given by Equation (6):

$$v_r = \frac{v_t^2}{r}\frac{\Delta\rho\pi}{\frac{18\mu\pi}{x_o^2} - 6k\rho_w\omega} \quad (6)$$

Ignoring the Magnus force in the calculations, the force balance equation of the oil droplet is written as Equation (7):

$$\sum F = F_p - F_a - F_s \quad (7)$$

where the differential form of this equation is given by Equation (8):

$$\frac{dv_r}{dt} = \frac{v_t^2}{r}\frac{\Delta\rho}{\rho_o} - \frac{18v_r\mu_w}{x_o^2\rho_o} \quad (8)$$

The relative radial velocity is given by Equation (9):

$$v_r = k\frac{v_t^2}{r}\frac{\Delta\rho x_o^2}{18\mu_w} \quad (9)$$

where k is the correction coefficient having the value of 0.02239 in the current work. Equations (5) and (9) indicate that for a fixed droplet size, the smaller the rotation radius (r), the greater the radial velocity of the oil droplet regardless of the consideration of random force. Moreover, for a constant rotation radius, the larger the diameter (x) of the oil droplet, the greater the radial velocity of the oil droplet.

Substituting $v_r = \frac{dr}{dt}$ and $v_t = \omega \cdot r$ into Equation (8), Equation (10) is obtained:

$$\frac{d^2r}{dt^2} + \frac{18\mu_w}{x_o^2\rho_o}\frac{dr}{dt} - \frac{\Delta\rho}{\rho_o}\omega^2 r = 0 \quad (10)$$

For a certain angular velocity of the rotating flow field, the time required for the discrete phase oil droplet to settle to the axis at the radius "r" from the axis in the radial direction is given by Equation (11):

$$t = \frac{18\mu_w}{x_o^2\Delta\rho\omega^2}\ln r \quad (11)$$

Equation (11) shows that the larger the particle size of the discrete phase oil droplets in the rotating flow field, the greater the angular velocity during the rotation and the shorter the time required for the oil droplets to move to the axis of the flow field at the same position from the axis.

Assuming that the oil drop moved in the Stokes region, the differential equation form of the motion in the rotating flow field is given by Equation (12):

$$m_{\mathrm{o}}\frac{dv_{\mathrm{r}}}{dt}+F_{\mathrm{a}}-F_{\mathrm{p}}+F_{\mathrm{s}}=0 \tag{12}$$

where the influence of the Magnus force on the oil drop is ignored. Equation (12) can be rewritten as Equation (13):

$$m_{\mathrm{o}}\frac{dv_{\mathrm{r}}}{dt}+3\pi\mu_{\mathrm{w}}v_{\mathrm{r}}x-m_{\mathrm{o}}\frac{\Delta\rho}{\rho_o}a=0 \tag{13}$$

where a is the tangential acceleration of the flow field. For a constant tangential acceleration a, the relative velocity is given by Equation (14):

$$v_r=\frac{\Delta\rho}{\rho_{\mathrm{o}}}\tau^*(1-e^{-\frac{t}{\tau^*}})a \tag{14}$$

where t is the time it takes for the oil droplet to reach 99.9% of the equilibrium velocity (s), and τ^* is a parameter that depends on the droplet size, density, and viscosity and is defined as Equation (15):

$$\tau^*=\frac{x_{\mathrm{o}}^2\rho_{\mathrm{o}}}{18\mu_{\mathrm{w}}} \tag{15}$$

The radial motion of the oil droplet in the rotating flow field can be divided into the acceleration stage and the constant velocity stage. After the acceleration stage, the oil droplet reached the equilibrium velocity, which is given by Equation (16):

$$v_r=\frac{\Delta\rho}{\rho_{\mathrm{o}}}\tau^*a=\frac{x_{\mathrm{o}}^2\Delta\rho}{18\mu}a \tag{16}$$

In the rotating flow field, the density of discrete and continuous phases was found to be 840 kg/m^3 and 1000 kg/m^3, respectively, and the continuous phase viscosity was 1.02 mPa·s. Applying these parameters to Equation (15) yielded the corresponding τ^* values of oil droplets with different particle sizes. Then, the migration time required for different oil droplets to reach 99.9% of the equilibrium velocity could be obtained, and the results are shown in Figure 10. The parameter reflected the time required for the oil droplet to move from the acceleration stage to the constant velocity stage in a radial motion. It was observed that the acceleration time of the particle size of 100 μm in the rotating flow field was about 0.004 s, whereas the acceleration time increased with the increase in particle size. When the particle size was 1500 μm, the acceleration time of the oil droplet was about 0.6 s. Meanwhile, Equation (14) indicates that when the oil droplet moves at a constant velocity in the radial direction, the larger the diameter of the oil droplet, the greater the equilibrium velocity.

3.3. Experimental Study on the Settling Process of Oil Droplets with Different Particle Sizes

The captured images were analyzed using the I-Speed software suite. To this end, several groups of oil droplets with different particle sizes were randomly selected. Initially, the droplets were spherical and broken by the rotor during the motion. During the process, the pixel size corresponding to the oil droplet diameter and the center of mass from the end of the radial migration position (equilibrium position) of the oil droplet was measured. Some target oil droplets were selected to describe the process from the initial position to the equilibrium position in the swirling field. To simplify counting the tracked oil droplets and show their position and morphology more clearly, the background of the keyframe image of the oil droplets' motion was removed and the contour recognition process was carried out. Figure 11 shows some keyframes in the separation process after the recognition of the contour. It was observed that the oil droplet rotated around the axis of the gas core from the initial position, and the rotational radius gradually decreased until it reached an equilibrium position. Then, the droplet wound around the surface of the gas core.

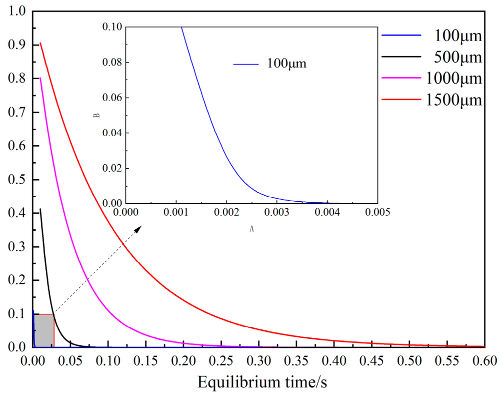

Figure 10. Comparison of the equilibrium time of oil droplets with different particle sizes.

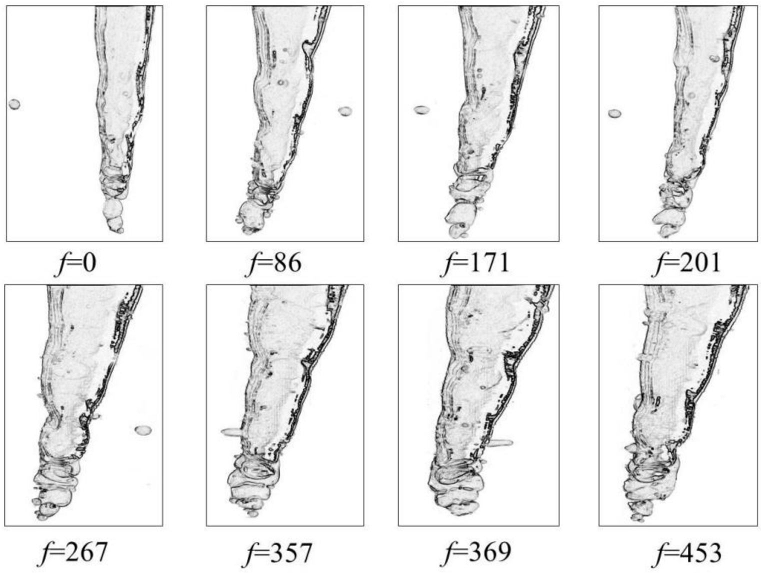

Figure 11. Separation process of 1# oil droplet.

Similarly, the separation of the other oil droplets was analyzed, the balance times were obtained, and the average radial velocity of the oil droplets was calculated according to the distance from the equilibrium point. The obtained results are presented in Table 1.

Table 1. Balance parameters of the oil droplets.

Oil Droplet	Oil Droplet Size/mm	Radial Position/mm	Balance Time/s	Average Radial Velocity/m·s^{-1}
1#	2.67	19.93	0.902	0.0221
2#	4.11	22.57	1.002	0.0225
3#	6.61	39.79	0.784	0.0531
4#	2.95	21.35	1.660	0.0219
5#	2.71	30.21	1.514	0.0200
6#	4.10	38.43	2.226	0.0173
7#	4.39	20.50	0.752	0.0273

To compare the experimental data with the results obtained from theoretical analyses, the radial velocity was used as the evaluation index. In this regard, oil droplets 1# and 5#, and droplets 2# and 6# were compared. These pairs of droplets had similar diameters but different radial distances. Meanwhile, the oil droplets 1# and 7# and droplets 3# and 6#

were close to the equilibrium points and had different particle sizes. Finally, oil droplets 1# and 7# and droplets 3# and 6# were compared in the same radial position.

First of all, the position of the seven oil droplets from the equilibrium point and the oil droplet size tracked in Table 1 were placed in Equation (11). The obtained distribution of the motion time of oil droplets with different particle sizes and angular velocity in the rotating flow field (shown in Figure 12) indicated that the radial movement time of the oil droplets decreased with the increase in the angular velocity in the rotating flow field. The obtained results showed that for the same angular velocity and distance, the larger the particle size, the shorter the movement time.

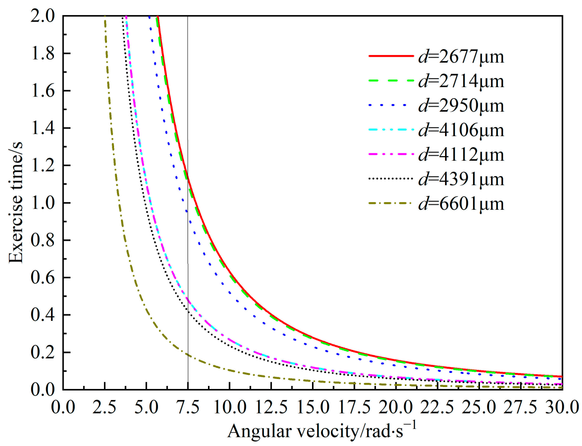

Figure 12. Theoretical values of the motion times of targeted oil droplets against the angular velocity.

Oil droplets 1# and 5# and droplets 2# and 6#, which had similar grain diameters and different radial distances, were compared. The equilibrium parameters of the oil droplets were placed in Equation (9) to compare the approximate theoretical values of the radial velocities of the oil droplets with the same particle size and different radial distance in the rotating flow field. The corresponding results are shown in Figure 13. The results showed that the closer the position to the equilibrium point, the higher the oil droplet velocity to the balance position of the axis. This was because the eddy current in the studied rotating flow field was generated by the high-speed rotation of the axial magnetic rotor. Therefore, the closer to the axis, the greater the tangential rotation velocity of the flow field and the greater the radial settling velocity of the oil droplet. The comparison of oil droplets 1# and 5# and droplets 2# and 6# was conducted, and the results are shown in Figure 13. It was found that the radial velocity of oil droplet 2# was obviously higher than that of droplet 6#, and the radial velocity of oil droplet 1# was higher than that of droplet 5#. In the rotating flow field and for a constant oil droplet diameter, the smaller the radial distance, the greater the radial velocity of the oil droplet. A similar trend was observed in the experimental results and theoretical analysis.

The oil droplets 1# and 7# and droplets 3# and 6#, which were close to the equilibrium point and had different particle sizes, were compared. These four groups of parameters were introduced into Equation (9) to obtain a comparison of the radial velocity of different oil droplet sizes in the rotating flow field. As shown in Figure 14, when the distance from the equilibrium position was small, the radial velocity of the oil droplet 7# with a larger particle size was higher than that of droplet 1#, whereas the radial velocity of oil droplet 6# was obviously higher than that of droplet 3#. To compare the experimental data and theoretical values, the results for different particle sizes at the same distance are shown in Figure 14. It was found that the radial velocities of oil droplets 6# and 7# with larger particle sizes were significantly higher than those of oil droplets 3# and 1#, indicating that the larger the droplet, the shorter the settling time and the larger the average radial velocity.

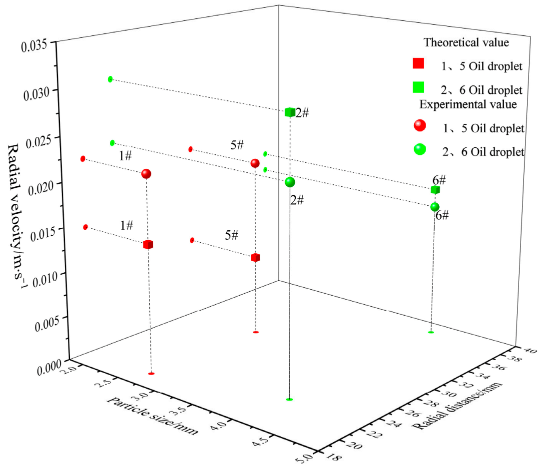

Figure 13. Comparison of theoretical and experimental values of the radial velocity of oil droplets with different radial distances in the rotating flow field.

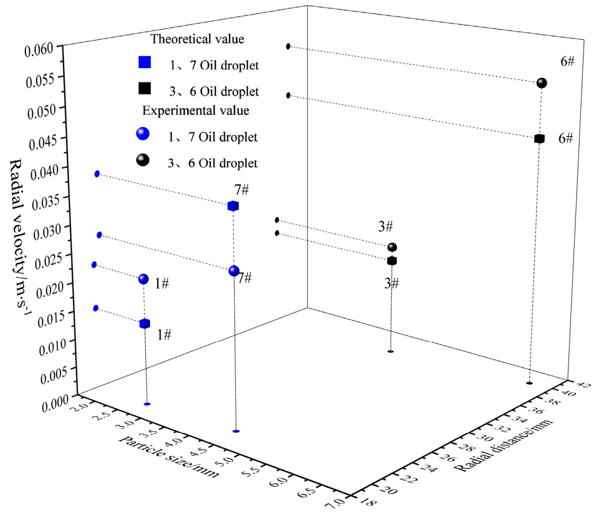

Figure 14. Comparison of theoretical and experimental values of the radial velocity of oil droplets with different radial distances in the rotating flow field.

4. Conclusions

In the present study, the migration of oil droplets in a rotating flow field was studied, and the influence of the agglomeration of the droplets on the separation process was analyzed by combining theoretical analysis and PIV measurements. Based on the obtained results and the performed analyses, the main achievements of this article can be summarized as follows.

(1) The distribution of the velocity field in an axially driven three-dimensional rotating flow field was obtained. There was a derived eddy current along the radial and axial directions, which was due to the random characteristics of the flow field. Moreover, the exponential function of tangential velocity varied with the radial distance at different velocities. It was found that with the gradual increase in the rotor speed, the velocity of the gas core disturbance zone increased with the increase in the gas core. Meanwhile, the velocity of the stable zone increased gradually, and the tangential velocity of the stable zone decreased with the increase in the distance from the axis.

(2) When the rotational speed of the magnetic agitator was 1020 r/min, the radial distance from the axes was 19.93 and 20.50 mm and the diameters of the oil droplets were 2.677 and 4.391 mm, respectively. Meanwhile, the equilibrium times of reaching the axis were 0.902 and 0.752 s, respectively. For the same angular velocity, the larger the particle

size, the shorter the moving time at the same distance. The radial distances from the axis of the two oil droplets with the diameters of 2.677 and 2.714 mm were 19.93 and 30.21 mm, respectively, and the corresponding radial velocities were 0.0221 and 0.02 $m \cdot s^{-1}$, respectively. The smaller the radial distance of the oil droplet, the greater the radial velocity of the oil droplet.

(3) For a constant rotational speed and medium, the settling velocity of the oil droplets was a function of the radial distance from the axis and the droplet size. At the same position, the larger the oil droplets, the shorter the time required to reach the equilibrium point and the larger the radial velocity. For the same oil droplet size, the smaller the radial distance, the greater the radial velocity of the oil droplet. In this regard, a mathematical expression was established between the settling time and the radial position of the oil droplets. The accuracy of the expression was verified using experiments.

The study of the deformation mechanism of oil droplets in a rotating flow field is also an ongoing and intriguing investigation direction, and we are conducting in-depth research in this area for future exploration.

Author Contributions: All authors contributed to the study and design. L.X. wrote the main manuscript text. S.G. prepared Figures 1–14. M.J. and Y.G. designed the whole experiment. All authors have read and agreed to the published version of the manuscript.

Funding: This work was supported by the key projects supported by the Regional Innovation and Development Joint Fund of the National Natural Science Foundation of China under grant number U21A20104 and the Project of Natural Science Foundation of Heilongjiang Province under grant number LH2022E017.

Data Availability Statement: Data are available on request due to restrictions, e.g., privacy or ethical. The data presented in this study are available on request from the corresponding author.

Conflicts of Interest: The authors declare no conflict of interest.

References

1. Song, M.; Zhao, L.; Xu, B.; Liu, L.; Zhang, S. Discussion on deep improvement technology of separation efficiency of liquid-liquid hydrocyclone. *Prog. Chem. Ind.* **2021**, *40*, 6590–6603.
2. Zhang, H.; Lu, Y. Numerical simulation of two-phase flow characteristics in supercritical water circulating fluidized bed. *J. Eng. Thermophys.* **2018**, *39*, 127–132.
3. Chen, A.; Huang, Q.; Geng, S.; Yang, C. Hydrodynamic characteristics of gas-liquid two-phase flow in jet reactor. *Prog. Chem. Ind.* **2018**, *37*, 1257–1266.
4. He, M.; Wang, N.; Hou, Q.; Chen, M.; Yu, H. Coalescence and sedimentation of liquid iron droplets during smelting reduction of converter slag with mechanical stirring. *Powder Technol.* **2020**, *362*, 550–558. [CrossRef]
5. Denisova, M.O.; Kostarev, K.G. Droplet Deformation under Conditions of Neutral Buoyancy. *J. Phys. Conf. Ser.* **2021**, *1945*, 012002. [CrossRef]
6. Solsvik, J.; Jakobsen, H.A. Single Air Bubble Breakup Experiments in Stirred Water Tank. *Int. J. Chem. React. Eng.* **2015**, *13*, 477–491. [CrossRef]
7. Schütz, S.; Gorbach, G.; Piesche, M. Modeling fluid behavior and droplet interactions during liquid-liquid separation in hydrocyclones. *Chem. Eng. Sci.* **2009**, *64*, 3935–3952. [CrossRef]
8. Xia, H. Study on the characteristics of oil droplet aggregation and migration in the swirling flow field of non-Newtonian fluid. *Northeast. Univ. Pet.* **2021**. [CrossRef]
9. Xing, L.; Jiang, M.; Zhang, Y.; Xiong, F. Oil droplet aggregation and crushing characteristics in shaft guide cone hydrocyclone. *J. China Univ. Pet. (Nat. Sci. Ed.)* **2019**, *43*, 140147.
10. Dalgamoni, H.N.; Yong, X. Numerical and theoretical modeling of droplet impact on spherical surfaces. *Phys. Fluids* **2021**, *33*, 052112. [CrossRef]
11. Yuan, S.; Liu, T.; Fan, Y.; Song, G.; Liu, J. Numerical simulation of droplet collision dynamics in oil-water separation process. *Petrochem. Ind.* **2021**, *50*, 675–679.
12. Wu, X.; Wei, N.; Liu, P.; Li, X.; Pan, H.; Li, H. Experimental study on bubble motion characteristics under different nozzle immersion modes. *J. Eng. Thermophys.* **2021**, *42*, 143–154.
13. Zhang, H.; Han, Z.; Wang, X.; Liu, H. Simulation of solid particle trajectory in cyclone separator based on DPM. *Shandong Chem. Ind.* **2020**, *49*, 127–129.
14. Solsvik, J.; Jakobsen, H.A. Single drop breakup experiments in stirred liquid–liquid tank. *Chem. Eng. Sci.* **2015**, *131*, 219–234. [CrossRef]

15. Liu, H.; Lu, Y.; Li, S.; Yu, Y.; Sahu, K.C. Deformation and breakup of a compound droplet in three-dimensional oscillatory shear flow. *Int. J. Multiph. Flow* **2021**, *134*, 103472. [CrossRef]
16. Ling, C.; Zhong, Y.; Peng, L. Three-dimensional numerical research on the effects of lateral pulsating airflow on droplet breakup. *Phys. Fluids* **2021**, *33*, 033303. [CrossRef]
17. Sun, G.; Liu, Y.; Lu, H.; Yang, Q.; Liu, H.; Zhu, Y. Study on the deformation and motion of oil droplets under the action of shear flow. *J. Jiangsu Univ. Sci. Technol. (Nat. Sci. Ed.)* **2019**, *33*, 41–47.
18. Bhardwaj, S.; Dalal, A.; Biswas, G.; Mukherjee, P.P. Analysis of droplet dynamics in a partially obstructed confinement in a three-dimensional channel. *Phys. Fluids* **2018**, *30*, 102102. [CrossRef]
19. Xing, L.; Gao, J.; Jiang, M.; Li, F.; Li, J.; Han, G. Application and comparison of coalescence and breakage model in hydrocyclone simulation. *Chem. Eng.* **2021**, *49*, 46–51.
20. Li, X.; Yuan, H. Study on the mechanism of droplet aggregation in hydrocyclone. *Min. Mach.* **2006**, *7*, 67–69.
21. Chen, D.; Wei, Z.; Jiang, M.; Zhao, L. Effect of large cone gas injection on separation performance of liquid-liquid hydrocyclone. *Chem. Mach.* **2014**, *41*, 480–483.
22. Wang, Z.; Ma, Y.; Jin, Y. Numerical simulation of oil droplet movement and migration in guide vane hydrocyclone. *J. Chem. Eng. Univ.* **2011**, *25*, 543–546.
23. Xu, Y.; Lin, K.; Wu, Z.; Lv, F.; Zhang, J. Numerical simulation of flow field in cyclone separator based on RSM and LES turbulence model. *Chem. Mach.* **2015**, *42*, 409–412, 446.
24. Xie, X.D.; Wang, X.C.; Wang, J.Z.; Li, Y.; Wang, J.; Guo, L.; Han, J.; Gu, J. Study on gas-liquid separation characteristics of cylindrical cyclone under low inlet void fraction. *J. Eng. Thermophys.* **2021**, *42*, 2873–2878.
25. Shi, B.; Xue, K.; Pan, J.; Zhang, X.; Ying, R.; Wu, L.; Zhang, Y. Liquid/solid flow field in a centrifugal pump with different impeller blade types by PIV. *Meas. Control* **2021**, *54*, 1219–1233. [CrossRef]
26. Gao, B.; Coltman, E.; Farnsworth, J.; Helmig, R.; Smits, K.M. Determination of vapor and momentum roughness lengths above an undulating soil surface based on piv-measured velocity profiles. *Water Resour. Res.* **2021**, *57*, e2021WR029578. [CrossRef]
27. Wang, X.B.; Liu, Y.; Cui, H.Q.; Han, H.S. A PIV experimental study on fluid flow characteristics in hydrocyclone. *Acta Petrol. Sin.* **2022**, *33*, 143–149.
28. Li, X.; Yuan, H.; Cao, Z. Analysis of mechanical characteristics of dispersed phase particles in swirl field. *Metal. Mine* **2007**, *101–103*, 134.
29. Xing, L. Study on the Migration Trajectory of Oil Droplets in a Swirl Field. *Northeast. Univ. Pet.* 2017. Available online: https://kns.cnki.net/kcms2/article/abstract?v=3uoqIhG8C475KOm_zrgu4lQARvep2SAkkyu7xrzFWukWIylgpWWcEg9jkstg9Dp9jlwR8hWWhhgupdcqi49zbJjPn7eMZbvF&uniplatform=NZKPT (accessed on 24 May 2023).
30. Qian, Y.; Li, J.; Ma, Y.; Yin, J.; Wang, D.; Li, H.; Liu, W. Numerical simulation of tritiated bubble trajectory in a gas-liquid separator. *Int. J. Energy Res.* **2018**, *42*, 293–302. [CrossRef]
31. Huang, Y.; Wang, H.; Tian, J.; Li, J.; He, F. Theoretical study on centrifugal coupling characteristics of self-rotation and revolution of particles in hydrocyclones. *Sep. Purif. Technol.* **2020**, *244*, 116552. [CrossRef]
32. Sandulyak, A.V.; Sandulyak, D.A.; Polismakova, M.N.; Ershova, V.A. Role of viscosity and temperature factors in the magnetophoresis of dispersed phase of different liquid media. *J. Eng. Phys. Thermophys.* **2021**, *94*, 919–926. [CrossRef]
33. Ozturk, D. Performance of a magnus effect-based cylindrical roll stabilizer on a full-scale motor-yacht. *Ocean. Eng.* **2020**, *218*, 108247. [CrossRef]